From hydrogen to helium: the spectral evolution of white dwarfs as evidence for convective mixing

Tim Cunningham,* Pier-Emmanuel Tremblay, Nicola Pietro Gentile Fusillo, Mark Hollands and Elena Cukanovaite

Department of Physics, University of Warwick, Coventry CV4 7AL, UK

ABSTRACT

We present a study of the hypothesis that white dwarfs undergo a spectral change from hydrogen- to helium-dominated atmospheres using a volume-limited photometric sample drawn from the *Gaia*-DR2 catalogue, the Sloan Digital Sky Survey (SDSS), and the *Galaxy Evolution Explorer* (*GALEX*). We exploit the strength of the Balmer jump in hydrogen-atmosphere DA white dwarfs to separate them from helium-dominated objects in SDSS colour space. Across the effective temperature range from 20 000 to 9000 K, we find that 22 per cent of white dwarfs will undergo a spectral change, with no spectral evolution being ruled out at 5σ. The most likely explanation is that the increase in He-rich objects is caused by the convective mixing of DA stars with thin hydrogen layers, in which helium is dredged up from deeper layers by a surface hydrogen convection zone. The rate of change in the fraction of He-rich objects as a function of temperature, coupled with a recent grid of 3D radiation-hydrodynamic simulations of convective DA white dwarfs – which include the full overshoot region – lead to a discussion on the distribution of total hydrogen mass in white dwarfs. We find that 60 per cent of white dwarfs must have a hydrogen mass larger than $M_{\rm H}/M_{\rm WD} = 10^{-10}$, another 25 per cent have masses in the range $M_{\rm H}/M_{\rm WD} = 10^{-14}$–$10^{-10}$, and 15 per cent have less hydrogen than $M_{\rm H}/M_{\rm WD} = 10^{-14}$. These results have implications for white dwarf asteroseismology, stellar evolution through the asymptotic giant branch and accretion of planetesimals on to white dwarfs.

Key words: convection – techniques: photometric – stars: atmospheres – stars: evolution – white dwarfs.

1 INTRODUCTION

From models of stellar evolution it is generally considered that white dwarfs are born with canonical masses of hydrogen and helium, $M_{\rm H}/M_{\rm WD} \approx 10^{-4}$ and $M_{\rm He}/M_{\rm WD} \approx 10^{-2}$, where $M_{\rm WD}$ is the total mass of the white dwarf (Iben & Renzini 1983; Schoenberner & Weidemann 1983; D'Antona & Mazzitelli 1990), with more recent estimates providing a parametrization as a function of stellar mass (Althaus et al. 2015; Romero et al. 2017). These values are determined based on nuclear burning rates following the main-sequence lifetime of the progenitor to the white dwarf. Over some decades, however, analyses of pulsating white dwarfs and stars evolving through and beyond the asymptotic giant branch (AGB; Werner & Herwig 2006; De Gerónimo et al. 2018), as well as population studies of cool white dwarfs (Tremblay & Bergeron 2008; Rolland, Bergeron & Fontaine 2018; Blouin et al. 2019), have led to the understanding that this is in all likelihood an upper limit on the mass of hydrogen. There has been much interest in constraining the mass of light elements in white dwarfs over the last few decades to understand their formation and evolution.

Pulsating DA stars (DAV or ZZ Cetis) provide the opportunity to probe the chemical structure of white dwarfs as they cool between ≈12 500 and 10 500 K (Tremblay et al. 2015). It is generally accepted that all (non-magnetic) DA stars will exhibit variability from non-radial g-mode pulsations, as they move through this temperature range during their evolution (Brickhill 1983, 1991; Bradley 1996; Fontaine & Brassard 2008). One of the great benefits of studying this population of white dwarfs is that models of asteroseismology describing the oscillatory behaviour are most sensitive to, among other parameters, the mass of the hydrogen layer (Fontaine & Brassard 2008). Predicted pulsation periods typically decrease when the hydrogen layer mass is increased, with the mean period spacing also decreasing slightly (Bradley 1996). Recent asteroseismological studies often require significantly smaller hydrogen masses than the canonical value ($\log M_{\rm H}/M_{\rm WD} \ll -4$) to allow matching observed and predicted g-mode pulsations (Giammichele et al. 2016; Romero et al. 2017).

* E-mail: t.cunningham@warwick.ac.uk

The small hydrogen masses that are invoked to model observed pulsations in some ZZ Cetis are thought to be explained by late hydrogen burning during the AGB and post-AGB (D'Antona & Mazzitelli 1990; Herwig et al. 1999; Werner & Herwig 2006; Althaus et al. 2010). Numerical simulations and theoretical calculations have shown that thermal pulses during and shortly after the AGB phase are able to burn up almost all of the remaining hydrogen (Straniero et al. 2003).

The radii of DA white dwarfs derived using evolutionary models with thin hydrogen layers are smaller than those with thick layers for a given mass (Wood 1990; Tremblay et al. 2017). Overestimating the hydrogen layer thickness can also lead to ages that are up to ≈1 Gyr too old for the coolest known white dwarfs (Fontaine, Brassard & Bergeron 2001). The field of Galactic archaeology has found white dwarfs to be useful chronometers in studies of the solar neighbourhood (Tremblay et al. 2014) and in determinations of the age of the Galactic disc (Winget et al. 1987; Wood 1990; Leggett, Ruiz & Bergeron 1998; Fontaine et al. 2001; Chen & Hansen 2012) or the Galactic halo (Kalirai 2012; Kilic et al. 2019). Providing an independent constraint on the occurrence of different hydrogen layer masses could help to improve the accuracy of these models.

As white dwarfs cool, the total amount of hydrogen and helium present, either primordial or accreted, can influence their subsequent evolution, and in particular their spectral appearance. The study of the spectral evolution of white dwarfs (Sion 1984; Fontaine & Wesemael 1987; Bergeron, Leggett & Ruiz 2001; Tremblay & Bergeron 2008) thus provides a method to learn about their past history and internal structure. In this work, we focus on the hydrogen content, although we note that the study of hot hydrogen-deficient PG1159 stars (Werner & Herwig 2006; Miller Bertolami 2016), carbon dredge-up in helium-rich atmosphere DQ white dwarfs (Pelletier et al. 1986; Coutu et al. 2019; Koester & Kepler 2019), as well as asteroseismology can also help to constrain the mass of helium.

After gravitational separation has occurred (Schatzman 1945), it is thought that hot white dwarfs will either cool as helium-rich DO atmospheres with He II lines, or hydrogen-atmosphere DA white dwarfs with Balmer lines if there is enough hydrogen to float at the surface. In both cases, radiative levitation can still keep trace metal species for ≈100 Myr, long after gravitational settling is complete (Chayer 2014; Koester, Gänsicke & Farihi 2014; Werner, Rauch & Kruk 2018). Both types of white dwarfs can also develop convective instabilities in their atmospheres or envelopes as they grow older, allowing for further changes in spectral types.

If a white dwarf has a thick enough hydrogen envelope ($\log M_{\rm H}/M_{\rm WD} \gtrapprox -14$; Rolland et al. 2018; Genest-Beaulieu & Bergeron 2019b), the convection zone will initially be confined to the hydrogen atmosphere. Recent numerical simulations have constrained the onset of convection in DA white dwarfs to arise at 18 000–18 250 K (Cunningham et al. 2019) which sets an upper limit on the temperature range over which convection can impact the evolution of these objects. As the convection zone grows with decreasing surface temperature, if the hydrogen layer is sufficiently small ($\log M_{\rm H}/M_{\rm WD} \lessapprox -6$), eventually the convection zone will reach the deeper helium layer (Fontaine et al. 2001). At this point, the significantly larger reservoir of helium ($\log M_{\rm He}/M_{\rm WD} \approx -2$) is expected to be immediately mixed into the surface convection zone in a runaway process resulting in a larger helium-dominated convection zone, a process named *convective mixing* (Strittmatter & Wickramasinghe 1971; Shipman 1972; Baglin & Vauclair 1973; Koester 1976). With convective velocities reaching $v \approx 1$ km s^{-1} the chemical profile will almost instantaneously become homogeneously mixed (Cukanovaite et al. 2018; Cunningham et al. 2019). The result will appear to be a helium-rich atmosphere white dwarf (DB spectral type with He I lines or DC type with no lines) that may have detectable hydrogen (DBA or DA spectral types; Rolland et al. 2018).

If a white dwarf has a thin enough total hydrogen mass ($\log M_{\rm H}/M_{\rm WD} \lessapprox -14$), a different evolutionary path is expected. Either the full evolution is in the form of a hydrogen-deficient PG1159, DO, DB, and then DC atmosphere (Genest-Beaulieu & Bergeron 2019b), or alternatively when the DO white dwarf reaches $T_{\rm eff} \approx 45\,000$ K it transforms into a DA with a very thin hydrogen atmosphere. Such a hydrogen layer is sufficiently small that the underlying helium layer is expected to become unstable to convection in the range $30\,000 \gtrapprox T_{\rm eff}/[{\rm K}] \gtrapprox 18\,000$ (MacDonald & Vennes 1991; Rolland et al. 2018; Genest-Beaulieu & Bergeron 2019b). Convective overshoot is then expected to rapidly mix the top hydrogen layer with the underlying small helium convection zone (Cukanovaite et al. 2019; Cunningham et al. 2019), resulting in the so-called *convective dilution* process. The result is a DB or DBA white dwarf like in the convective mixing process described above, albeit with a different range of possible hydrogen abundances (Genest-Beaulieu & Bergeron 2019b).

In principle, the hydrogen abundances in DBA stars could be used to reconstruct their past evolution, but this is not accounting for the fact that accretion of planetary debris can significantly impact their hydrogen content. In fact, several DBA white dwarfs have orders of magnitude more hydrogen than would be possible by the convective dilution or convective mixing scenarios, and it is thought that the accretion of water-rich asteroids is the most likely explanation for the hydrogen abundance in these objects (Farihi et al. 2011; Raddi et al. 2015; Gentile Fusillo et al. 2017). The study of spectral evolution is clearly complex and involves many competing models that need to be constrained with well-defined samples of the local white dwarf population.

Observational statistical studies on the number ratio of hydrogen- to helium-atmospheres as a function of temperature have mainly been carried out using spectroscopically identified samples with a magnitude limit (Bergeron, Ruiz & Leggett 1997; Bergeron et al. 2001; Tremblay & Bergeron 2008; Blouin et al. 2019; Ourique et al. 2019; Genest-Beaulieu & Bergeron 2019b) with the exception of Limoges, Bergeron & Lépine (2015) who relied on the volume-limited 40 pc sample. In particular, we note that studying spectral evolution with the Sloan Digital Sky Survey (SDSS) spectroscopic sample, the largest known such sample for white dwarfs (Kepler et al. 2019), involves complex completeness corrections that are still not fully understood (Gentile Fusillo, Gänsicke & Greiss 2015). Photometrically selected or volume-complete samples have a strong advantage because the selection effects are better understood, especially in light of the recent *Gaia*- DR2 (Gaia Collaboration et al. 2016, 2018).

In this work, we make use of *Gaia* and a new robust photometric technique to study spectral evolution for volume-complete white dwarf samples. We utilize a catalogue of ≈260 000 high-probability white dwarf candidates from *Gaia* (Gentile Fusillo et al. 2019) to select among them those with *ugriz* photometry from the SDSS (Blanton et al. 2017). The SDSS $u - g$ colour is sensitive to the Balmer jump in the range $20\,000 \gtrapprox T_{\rm eff}/[{\rm K}] \gtrapprox 9000$, allowing us to separate white dwarfs with hydrogen atmospheres (H-rich) from those with helium atmospheres (He-rich) without using the much more incomplete SDSS spectroscopic sample. Coupling photometric data from *Gaia*, SDSS, and *GALEX* with a grid of 3D radiation-hydrodynamic simulations of convective DA white dwarf

atmospheres (Tremblay et al. 2013; Cunningham et al. 2019), we study the scenario of convective mixing which is expected to happen within that temperature range. We investigate the mass distribution of hydrogen layers in white dwarfs with the highest precision to date, albeit within a limited mass range of $-14 \lessapprox \log M_{\rm H}/M_{\rm WD} \lessapprox -10$, given the $T_{\rm eff}$ range allowed to be studied with our technique.

We first describe our observed sample selection in Section 2. Section 3 discusses the atmospheric models used to fit the photometric and astrometric data for the determination of effective temperature and stellar mass. Section 4 highlights the key results from the investigation and Section 5 contextualizes the implications of our study.

2 PHOTOMETRIC SAMPLE

For this investigation, we chose a volume-limited sample of high-confidence white dwarfs using the *Gaia*- DR2 catalogue built by Gentile Fusillo et al. (2019). The selection criteria used were; a quality cut ($P_{\rm WD} \geq 0.75$) that returned 262 480 objects, a parallax cut (parallax $\geq$7.5 mas) returning 35 056 objects, an effective temperature range determined by fits to the *Gaia* parallax and photometry ($20\,000 \geq T_{\rm eff}/[{\rm K}] \geq 9000$) returning 6512 objects and a cross-match with the SDSS photometry that returned a final sample size of 2207 objects. We emphasize that a large fraction of these objects do not have SDSS spectra. The cut in effective temperature is not essential at this stage, but included to indicate the size of the working sample. In Section 4, the parallax cut is also relaxed to explore the results at greater distances and diagnose whether small number statistics can impact our results. All significant results, however, are borne from the sample with cuts detailed in the aforementioned.

In order to separate the hydrogen- and helium-dominated atmosphere white dwarfs from photometry alone, we exploit the Balmer jump discontinuity that can be observed in spectra from sources with $T_{\rm eff} \approx 8\,000$–$20\,000$ K. This discontinuity occurs at $\lambda \approx 364.4$–380.0 nm, depending on the stellar mass and strength of non-ideal effects (Hummer & Mihalas 1988), making the SDSS u and g filters (central wavelengths of 354.3 and 477.0 nm, respectively) ideally suited to detect this feature. As a comparison colour we use $g - r$ with the central wavelength of r at 623.1 nm. As an illustration, Fig. 1 shows the sub-sample of 690 objects with SDSS spectra in a $u - g$, $g - r$ colour–colour plot where spectroscopically classified DAs are shown with pink circles and non-DAs are shown with green squares. The convention used throughout is that DAs include magnetic (DAH) and metal-rich (DAZ) objects, whilst non-DAs comprise DB, DBA, DAB, DC, DQ, and all magnetic (H) and polluted (Z) variations therein.

Fig. 2 shows the full sample from the photometric *Gaia*-SDSS cross-match in an analogous plot where objects with a spectral classification are shown in pink (DA, DAH, DAZ) and green (non-DA), whilst objects with blue points have no spectroscopic classification.

Obtaining an immaculate separation of spectrally classified DA and non-DA objects is not feasible, with some DA objects (pink) occupying the same colour space as the strip of non-DA objects (green). An inspection of their spectra reveals that predominantly the DA-type objects in the He-rich region of the colour plot are He-rich DA or DAZ (Zuckerman et al. 2007; Tremblay, Bergeron & Gianninas 2011; Gentile Fusillo et al. 2017; Rolland et al. 2018). In these instances – where there is sufficient helium to suppress the Balmer jump – these objects are correctly positioned photometrically, despite being classified as DA. That these objects sit in the photometric He-rich region is apposite for our analysis of the H- to He-rich atmosphere ratio. However, there exists an area between the photometric clusters sparsely populated by objects that have an ambiguous atmospheric composition. To improve the separation, we employ additional photometry from *GALEX* which we discuss in the following.

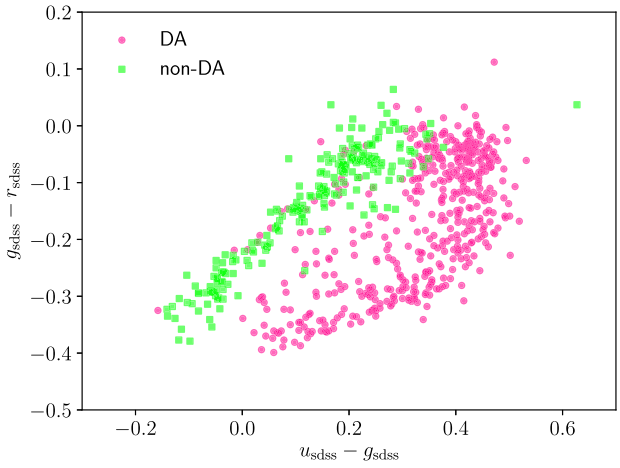

Figure 1 Colour–colour diagram showing 690 objects from the volume-limited white dwarf sample (parallax $\geq$7.5 mas) with a SDSS spectral classification (Gentile Fusillo et al. 2019). Of those shown, 479 are spectrally classified as DA (including DAH or DAZ) and 211 are classified as non-DA (including DB, DC, DQ, DBA, DAB, and all magnetic and polluted variants of the aforementioned) with pink (circles) and green (squares), respectively.

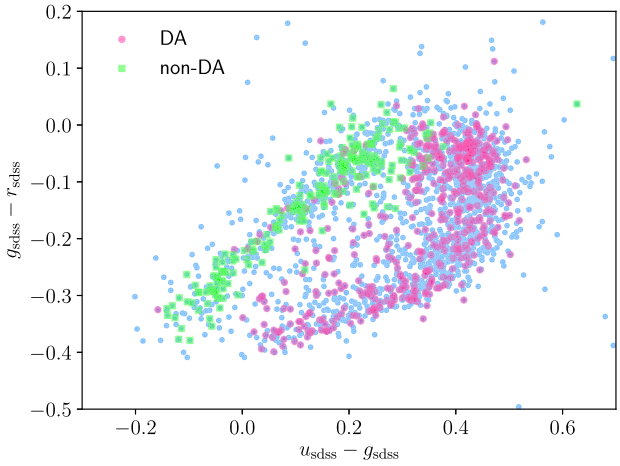

Figure 2 Colour–colour diagram showing 2207 objects (blue) from the volume-limited *Gaia*-SDSS photometric sample (parallax $\geq$7.5 mas). Of those shown, 479 are spectrally classified as DA (including DAH or DAZ) and 211 are classified as non-DA (including DB, DC, DQ, DBA, DAB and all magnetic and polluted variants of the aforementioned) in pink (circles) and green (squares), respectively. 74 objects from the full sample populate a region of colour space outside the axis range shown. A manual inspection of the SDSS catalogue revealed that $\approx$65 per cent of those objects had been marked with a CLEAN = 0 flag. The vast majority of all outliers are close to a bright star. We therefore remove these 74 objects from our sample.

2.1 *GALEX*

The all-sky survey *GALEX* (Morrissey et al. 2007) provides photometry in the near- and far-ultraviolet for a large number of

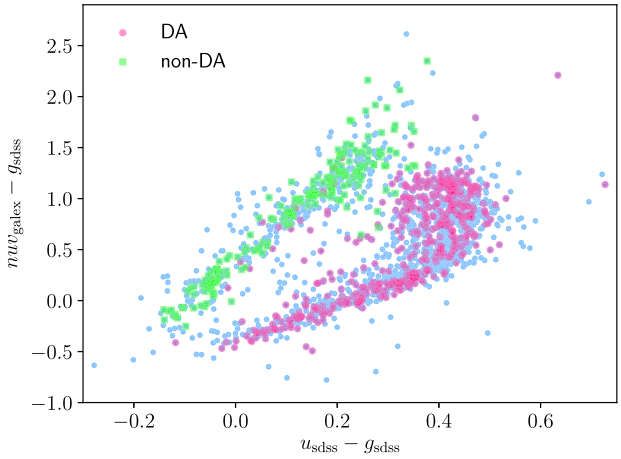

Figure 3 Similar to Fig. 2 but utilizing NUV from *GALEX*, which reduces the sample to 1781 objects (blue). Of those, 423 are spectrally classified as DA (pink circles) and 183 are classified as non-DA (green squares).

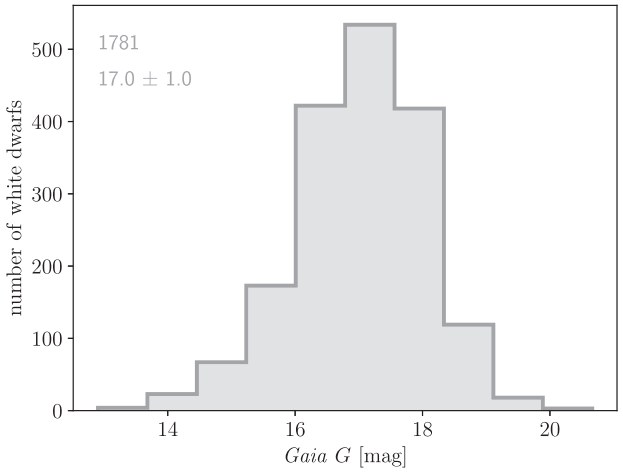

Figure 4 Distribution of *Gaia G* magnitudes for the 1781 objects included in our working sample after a cross-match with SDSS and *GALEX*. The mean magnitude is 17.0 with a standard deviation of 1.0.

objects in our sample. We find that the separation between the spectrally classified sources (Fig. 3) is increased when the colour $g - r$ (see Fig. 2) is replaced by $nuv - g$. The large majority of DA stars found in the He-rich cluster in colour space are He-rich DA white dwarfs, with only a handful of true contaminants (see Section 4). Approximately 400 objects in the sample were found to have unreliable or missing near-UV photometric data in *GALEX*, reducing the final working sample to 1781 high-confidence white dwarfs. Of those, 604 have SDSS spectral classifications as either DA[H,Z] (423) or non-DA (181).

2.2 Completeness

We have shown that it is possible to calculate the fraction of H- and He-rich atmosphere white dwarfs relying solely on *Gaia*, SDSS, and *GALEX* photometry for a limited $T_{\rm eff}$ range but it is also important to understand the completeness of this sample. A discussion on the completeness of the *Gaia*-SDSS photometric sample is in Section 6 of Gentile Fusillo et al. (2019) and summarized below. We emphasize that these authors also derive a *Gaia*-SDSS spectroscopic sample (their Section 5), which is separate and not as complete since SDSS used complex surveying strategies to follow-up their photometric sources (see e.g. Eisenstein et al. 2006). In Figs 1–2 and Section 4, we use this spectroscopic sample as a guide and comparison to our main photometric results. However, it is outside of the scope of this work to review the completeness of the spectroscopic *Gaia*-SDSS sample, which is known to vary considerably within colour–colour space, hence with $T_{\rm eff}$ and spectral type (Gentile Fusillo et al. 2015, 2019), and very likely impacting DA to non-DA ratios. Most earlier studies on spectral evolution have used such spectroscopic samples, although not as complete as with the selection defined in Gentile Fusillo et al. (2019). As a consequence we do not attempt to quantify the differences between these earlier studies and our method until spectroscopic completeness is better understood. Volume-complete spectroscopic samples, e.g. within 40 pc (Limoges et al. 2015), still suffer from low number statistics in the $T_{\rm eff}$ range we are interested in.

In Gentile Fusillo et al. (2019), the authors estimated the completeness of the *Gaia*-SDSS photometric cross-match based on the number of objects from the SDSS that were successfully retrieved by *Gaia*. They found that for white dwarfs with $G \leq 20$ and $T_{\rm eff} \geq 7\,000$ K, *Gaia* catalogued 60–85 per cent of the objects in the fairly complete SDSS footprint (sky images). However, this includes white dwarfs at faint magnitudes and large distances that are too far to have a detectable parallax in *Gaia*. Given that our sample only includes objects within 133 pc we expect the completeness of the cross-match to be much higher than this estimate. In fact, Hollands et al. (2018) find that the *Gaia* completeness is near 99 per cent for white dwarfs at 20 pc, and Gentile Fusillo et al. (2019) argue that there is no reason for this completeness to drop significantly within $\approx$100 pc and for $G < 20$ mag. Most importantly, Gentile Fusillo et al. (2019) also quantified the completeness with respect to $u - g$ colour using the SDSS filters and found it to be colour independent (see their fig. 18). This is a key parameter that makes our photometric method potentially more robust than earlier spectroscopic studies.

The SDSS footprint covers approximately one third of the sky meaning our sample is volume-limited only over the SDSS footprint. Within the distance set by the parallax cut our sample should be representative of the whole sky. The SDSS has a bright magnitude limit, with most white dwarfs brighter than $G \approx 15$ missing from the cross-match. Our sample is therefore not truly volume-limited. Our final magnitude distribution peaks at $G = 17.0$ with a standard deviation of 1.0 (Fig. 4) and, with 70 of the 1781 objects having $G < 15$, we infer that we are likely missing no more than $\approx$ 4 per cent of all objects which is not expected to introduce a significant DA versus non-DA bias (see Section 2.3).

The final sample uses a further cross-match with *GALEX*, and as such the completeness of *GALEX* is also important. To assess whether the inclusion of *GALEX* photometry introduces any bias within our sample, we consider the colour distributions for the percentage of objects in the original SDSS sample that were also retrieved during the *GALEX* cross-match. Fig. 5 shows the distributions for $u - g$ (blue, hatched) and $g - r$ (orange, solid) colours for the final working sample. We find no significant colour dependence for objects found in the *GALEX* cross-match, where all bins are consistent with an $\approx$80 per cent retrieval rate to within 1σ.

We also show the distribution of objects recovered in the *GALEX*-SDSS cross-match as a function of distance (Fig. 6) to investigate whether any spatial bias could have been introduced. The distance is inferred using the *Gaia* parallax and we find the recovery rate of objects in *GALEX* shows no dependence on this parameter. As with the colour distributions, we find all bins are consistent with

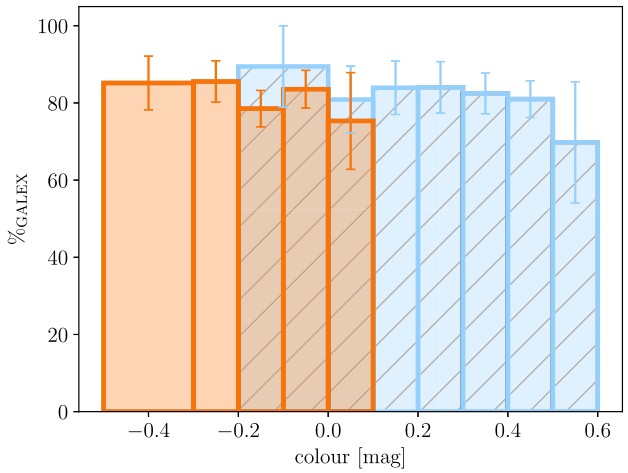

Figure 5 Colour distributions of percentage of SDSS objects (Fig. 2) recovered during the *GALEX* cross-match. In blue is the $u - g$ distribution for objects with colours from −0.2 to 0.6 mag. In orange, we show the $g - r$ distribution for objects with colours from −0.5 to 0.1 mag. The colour ranges encompass the full extent of the locus of points in Fig. 2.

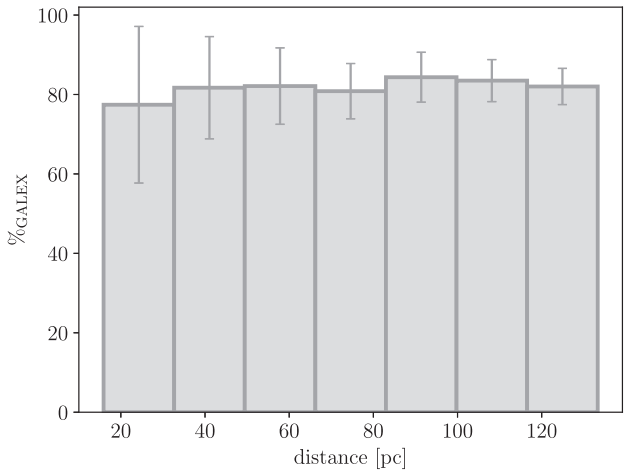

Figure 6 Distance distribution, inferred from *Gaia* parallax, of the percentage of the SDSS sample (Fig. 2) recovered during the *GALEX* cross-match.

a retrieval rate of 80 per cent to within 1σ. We conclude that the volume completeness of the final, working sample is likely to be 80 per cent that of the original SDSS sample and that no bias has been introduced as a result of including *GALEX* photometry. Given the SDSS bright magnitude limit and our $T_{\rm eff}$ range, our *GALEX* sources do not suffer significantly from non-linearity problems (Camarota & Holberg 2014; Wall et al. 2019).

Finally, we note that given our lower temperature limit of 9000 K and the lower magnitude limits of *Gaia*, SDSS, and *GALEX*, our distance limit of 133 pc ensures that a negligible amount of white dwarfs are removed for being too faint in any of the surveys. At 9000 K *Gaia* is the limiting survey and Fig. 4 illustrates that our distribution peaks well above the lower magnitude limit of $G \approx 20$.

2.3 Absolute magnitudes and cooling rates

The use of a volume-limited sample largely removes possible selection biases due to absolute magnitude differences between spectral types, but this concern still applies because of the bright

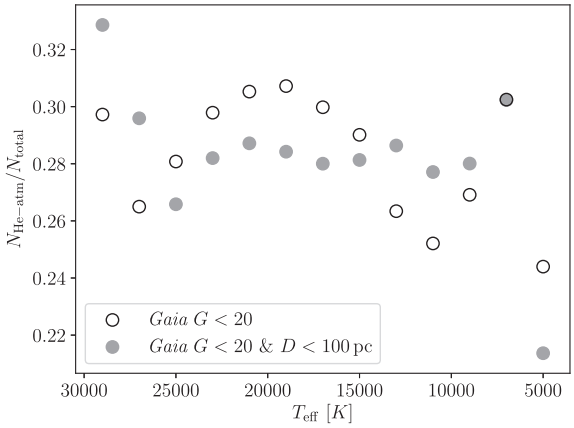

Figure 7 Simulated temperature dependence of the helium-dominated white dwarf fraction for volume (open circles) and magnitude limited samples (filled circles), assuming no spectral evolution at any time during the evolution. Input at birth included 72 per cent H-rich and 28 per cent He-rich atmospheres. The coolest bin is affected by the age of the Galactic disc and collision-induced opacities and should be interpreted with caution (Blouin et al. 2019).

magnitude limit of the SDSS. In addition, a difference in the cooling rates of DA and DB stars could influence the ratio of spectral types as a function of temperature. To understand these biases, we have simulated *Gaia* samples using the methods outlined in Tremblay et al. (2016) and Gentile Fusillo et al. (2019). These simulations assume a stellar formation rate (Tremblay et al. 2014), the Salpeter initial mass function, the Cummings et al. (2016) initial-to-final mass relation, and the white dwarf evolution models of Fontaine et al. (2001). Most importantly, 28 per cent of the white dwarfs are born with He-atmospheres (all with thin hydrogen layers), and 72 per cent with hydrogen atmospheres (where among those 14 per cent have thin hydrogen layers). In the subsequent evolution no spectral change is allowed. To eliminate random noise the white dwarf space density was artificially enhanced. Fig. 7 demonstrates that for a volume-limited sample, differences in cooling rates lead to small few per cent-level changes of spectral type ratio over time. For reference, Fig. 7 also shows the evolution for a magnitude-limited sample, where differences in absolute magnitude between DA and DB also play a role in the observed ratio. Once again, the effect from these biases is fairly minor, as outlined in Tremblay & Bergeron (2008). We conclude that any significant change (> 2 per cent) in the observed $N_{\rm He}/N_{\rm Tot}$ ratio, in the range of 20 000 $\gtrapprox T_{\rm eff}$/[K] $\gtrapprox$ 9000 and for a volume-limited sample, must be caused by additional physical processes that happen during white dwarf evolution and that are not included in our simulations, such as convective mixing or accretion.

3 ATMOSPHERIC COMPOSITION

Using *Gaia* photometry and astrometry, most high-probability white dwarfs in the DR2 catalogue of Gentile Fusillo et al. (2019) have a derived effective temperature from a dereddening procedure and model atmosphere calculation under the assumption of either a pure-hydrogen or a pure-helium atmosphere. The catalogue also makes use of the mass–radius relation of Fontaine et al. (2001) to derive a mass for each object.

The authors showed that, for a sample of 4778 bright DA stars, the $T_{\rm eff}$ determinations using *Gaia* photometry were in agreement

with those derived independently utilizing photometry from SDSS and Pan-STARRS.

Tremblay et al. (2019) and Genest-Beaulieu & Bergeron (2019a) also made a comparison of photometric and spectroscopic effective temperatures derived from the SDSS. Individual objects were in agreement to within 1–2σ, but spectroscopic temperatures were systematically higher than those derived from *Gaia* photometry. It was concluded that this was most likely due to residual issues with the spectroscopic temperature scale.

Bergeron et al. (2019) have shown that using pure-He models in the photometric technique for objects below $T_{\rm eff} \approx 11\,000$ K results in a systematic effective temperature and mass offset compared to mixed H/He models (see their figs 10 and 11). In the following section, the ratio of He- and H-rich objects – calculated from the SDSS-*GALEX-Gaia* photometric sample and empirical cuts described below – is computed using $T_{\rm eff}$ bins of 1000 K. Hence, the systematic offset in $T_{\rm eff}$ and mass is not a significant concern for this analysis.

The cuts in $u-g$, $g-r$ and $u-g$, $nuv-g$ space employed to optimize the separation between the spectrally classified objects in Figs 1–3 are given, respectively, by the following equations:

$$(g-r) = 0.8 \times (u-g) - 0.3, \quad (1)$$

$$(nuv-g) = 3.9 \times (u-g) - 0.1. \quad (2)$$

These empirical cuts are then used to estimate the ratio of H- to He-dominated atmospheres, below and above those lines, respectively. We then employ the *Gaia* photometric effective temperatures as described in Gentile Fusillo et al. (2019) to transform this ratio into the context of white dwarf spectral evolution. White dwarf cooling takes place over a Gyr time-scale (D'Antona & Mazzitelli 1990) and employing evolutionary models would allow the study of spectral evolution as a function of age. For simplicity, effective temperatures are used as a proxy for age in this study. We use the pure-H and pure-He solutions for the H-rich and He-rich sides of our colours cuts, respectively. We note that the differences between H- and He-rich effective temperature using *Gaia* photometry are sufficiently small compared to the size of our bins that even if pure-H effective temperatures were used for all objects similar results would be obtained.

4 RESULTS

For our derivation of the number of H- and He-atmospheres ($N_{\rm H\text{-}atm}$ and $N_{\rm He\text{-}atm}$), we devote our attention to the colour cut defined by equation (2) utilizing the near-ultraviolet from *GALEX*, which creates a cleaner separation than equation (1). The top left-hand panel of Fig. 8 shows the effect of the photometric cut, with objects on the hydrogen side coloured orange and those on the helium side coloured blue. This includes objects with spectral classification. Shown in black are the spectrally classified objects that apparently fall on the *wrong* side of the photometric cut with DA-type objects on the helium side (triangles) and non-DAs on the hydrogen side (circles). Of the 604 spectrally classified objects, we find 26 to be on the incorrect side of the cut. However, we point out that our goal is to separate H- and He-rich objects, rather than DA and non-DA.

We note that the misidentification is skewed towards DA-type objects with 5.2 per cent (22/423) of these objects on the He-rich side of the cut, compared to 2.2 per cent (4/183) for the non-DA types. An inspection of the spectra for the DA-type objects in the He-rich region finds the majority (16/22) are either He-rich DAs or DA+DC binaries (Rolland et al. 2018; Kepler et al. 2019), suggesting those objects may sit correctly in the photometric analysis. A further five objects on both sides show evidence of metal pollution or strong magnetic fields. Calcium lines in the former case can reduce the u-band flux (Hollands et al. 2017), emulating the Balmer jump, and strong magnetic fields can significantly disrupt the Balmer jump. The remaining five objects have $T_{\rm eff} \approx 9000$ K and higher-than-average surface gravities, where we expect the strength of the Balmer jump to be marginal. We conclude that H- and He-rich atmospheres separate relatively well under the photometric colour cut chosen, with 96–98 per cent of objects being assigned the correct composition.

The spectroscopic identifications serve as an indication of the photometric regions corresponding to hydrogen and helium dominance. Given a large enough and unbiased sample of spectra, one could study the atmospheric composition of each object in turn and model the spectral evolution in that fashion. With the small size or biases present in the current spectroscopic samples this is not a well-justified approach, which is why we focus our analysis on the photometric sample.

The top right-hand panel of the figure shows the photometric fraction, $N_{\rm He\text{-}atm}/N_{\rm total}$, as a function of effective temperature in bins of 1000 K. As a comparison the red dotted line shows the same quantity but only including objects with SDSS spectra, i.e. following the photometric cuts without regard to the actual spectral type. In this case we also rely on the photometric temperatures since some spectral types, e.g. DC, DZ, and DQ white dwarfs, have uncertain spectroscopic temperatures. Finally, this can be compared to the spectroscopic non-DA to total ratio in the same bins with the blue solid line. It demonstrates that the combined presence, as discussed above, of a few He-rich DA, strongly magnetic DAH, and DZ white dwarfs, only have a minor impact on our results.

The same analysis was carried out for increasing distance with a parallax cut of $\pi > 7.5$ (upper), 5.0 (middle), and 2.5 mas (lower) also shown in the figure. As photometric precision and volume completeness decrease with distance, we expect that our colour cut of equation (2) becomes less reliable to select atmospheric composition, and as such we favour the smaller volume photometric results. In contrast, larger distances may be able to overcome low number statistics for spectroscopic ratios, without necessarily adding more contaminants. The largest volume results in an approach that is closer to those of Genest-Beaulieu & Bergeron (2019b) and Ourique et al. (2019).

The errors associated with the photometric and spectroscopic ratios are derived from propagated Poisson errors by the expression

$$\alpha = \left(\left(\frac{n_{\rm He} + \alpha_{\rm He}}{n_{\rm tot}} - \frac{n_{\rm He}}{n_{\rm tot}} \right)^2 + \left(\frac{n_{\rm He}}{n_{\rm tot} + \alpha_{\rm tot}} - \frac{n_{\rm He}}{n_{\rm tot}} \right)^2 \right)^{1/2}, \quad (3)$$

where $n_{\rm tot}$ and $n_{\rm He}$ are, respectively, the total number of objects and inferred numbers of helium-dominated atmosphere white dwarfs from the photometry or spectroscopy and $\alpha_{\rm X} = \sqrt{n_{\rm X}}$ represents the counting (Poisson) error on both quantities.

Biases in the SDSS spectroscopic follow-up selection function, which depends on the SDSS colours (Gentile Fusillo et al. 2015), implies that the spectroscopic ratio may be less reliable. However, a comparison of the photometric and spectroscopic ratios for $\pi > 7.5$ mas finds them to be in agreement to within 1σ throughout the effective temperature range studied, with the exception of the bin centred at $T_{\rm eff} = 13\,500$ K. At larger distances, we observe a more prominent disagreement in the same temperature range.

The Poisson errors derived do not take into account the error on the effective temperature. We investigate the validity of the ex-

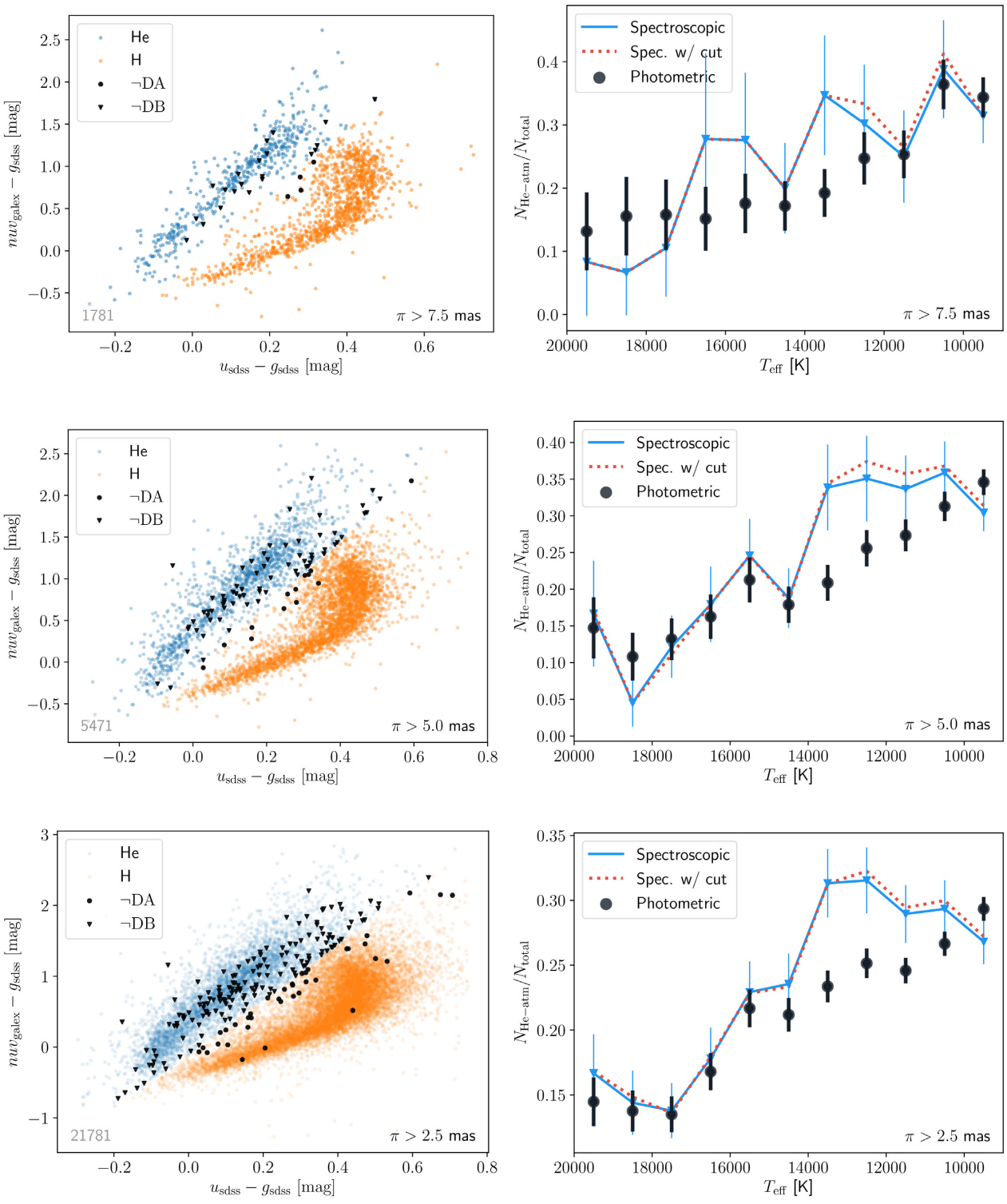

Figure 8 *Top-to-bottom*: Same analysis shown for samples limited by increasing volume with the parallax (bottom right) and sample size (bottom left) indicated in the panels. *Left*: Photometric sample with separation of colour space for hydrogen-dominated (orange) and helium-dominated atmospheres (blue) according to Fig. 3 and equation (2). Spectrally classified objects are a small subsample of the photometric sample. Any objects with a spectral classification that apparently disagrees with its photometric assessment are shown in black for DAs with photometry predicting He-dominance (triangles) and non-DAs with photometry indicating H-dominance (circles). *Right*: Ratio of helium-dominated objects to total as a function of effective temperature based on the photometric cuts (black circles). We also show the spectroscopic ratio in the same bins with (red, dotted) and without (blue, solid) respect for the photometric cut. Error bars result from the propagation of Poisson errors (see equation 3).

pressed error margin by calculating the sum of normal distributions in effective temperature for all objects in the top (the left-hand panel of Fig. 8). The normal distribution for species X (=H or He), $P_X(T_i)$, assigned to data point, i, obeys

$$P_X(T_i) = \frac{1}{\sqrt{2\pi}\sigma_i} \exp\left(\frac{(T - T_i)^2}{2\sigma_i^2}\right), \quad (4)$$

where T_i and σ_i represent the modelled effective temperature and associated error. An expression of the continuous ratio of He-rich to total objects would then be computed as

$$\frac{N_{\rm He-atm}}{N_{\rm total}} = \sum_{i=1} \frac{P_{\rm He}(T_i)}{P_{\rm H}(T_i) + P_{\rm He}(T_i)}. \quad (5)$$

We find that all error bars from the original histogram bins are intersected by this function, with the exception of the bin centred at $T_{\rm eff} = 10\,500$ K. We conclude that the errors attributed to the histogram bins from number statistics are a reasonable reflection of the uncertainty on the estimated photometric ratio.

4.1 Fitting the spectral evolution

One of the aims of this research is to model the observed spectral evolution. In order to do this we wish to express the fractional change of He-rich objects as a function of effective temperature. One could employ the values attributed to the histogram bins shown in the top left-hand panel of Fig. 8, where the local gradient is the quantity of interest. However, the local gradient of the He-rich fraction versus effective temperature in the histogram picture has some dependence on the choice of histogram bins. This is not conducive to a robust result and so we instead seek a continuous function of effective temperature.

Logistic regression is a well-established technique used in statistics and machine learning that estimates the likelihood of a function to describe a set of data, and it is increasingly being utilized in problems of an astrophysical nature (Hollands et al. 2018; Chromey 2019). We assume that at a given effective temperature, $T_{\rm eff}$, the probability of a white dwarf being He-rich is given by $S(\boldsymbol{\theta}, T_{\rm eff})$, where $\boldsymbol{\theta}$ is the vector of parameters that describe the form of function S – whose shape we would like to find. Given that our data are categorical – objects are either deemed to be H-rich or He-rich – logistic regression is an apposite choice for finding this function. We summarize the methodology in the following.

We define S in terms of the logistic curve:

$$S(\boldsymbol{\theta}, T_{\rm eff}) = \frac{1}{1 + \exp(-f(\boldsymbol{\theta}, T_{\rm eff}))}, \quad (6)$$

where the function f is defined as second-order polynomial in the natural logarithm of effective temperature such that

$$f(\boldsymbol{\theta}, T_{\rm eff}) = \theta_0 \log\left(\frac{T_{\rm eff}}{[K]}\right)^2 + \theta_1 \log\left(\frac{T_{\rm eff}}{[K]}\right) + \theta_2. \quad (7)$$

Defining S in this fashion ensures that the probability of an object being He-rich is confined to the interval [0,1]. This function differs from that used by Hollands et al. (2018) with the addition of the second-order term in the polynomial. Adopting this term gives the model the freedom not to tend to zero, which is important as we expect the He-rich fraction to be non-zero for all temperatures.

Now that we have a functional form with the freedom necessary to describe the likely shape of the probability of a white dwarf being He-rich, we invoke an optimization routine. The quantity we wish to maximize is the likelihood of the function S with parameters $\boldsymbol{\theta}$ being the best description of the data. Under the assumption that our

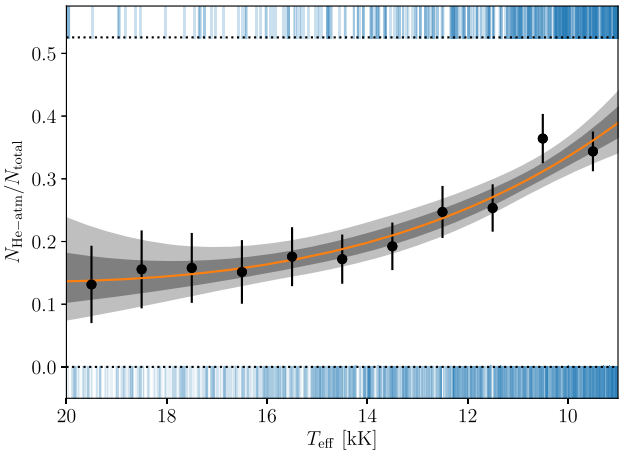

Figure 9 Observed fraction of helium atmosphere white dwarfs derived by the method of logistic regression using equation (6) and our $\pi > 7.5$ mas *Gaia*-SDSS-*GALEX* photometric sample. Filled error regions correspond to the 1σ and 2σ confidence intervals. Blue vertical lines indicate the effective temperature of a white dwarf with either a He-rich or H-rich atmosphere on the top and bottom, respectively. Photometric ratios derived using the binning method (see the top right-hand panel of Fig. 8) are also shown in black circles.

data is independently Bernoulli distributed – that data have either the value 1 or 0 – the likelihood of a given $\boldsymbol{\theta}$ describing the data is expressed as

$$L(\boldsymbol{\theta}|T_{\rm eff}) = \prod_{i=1}^{N} S_i^{y_i} (1 - S_i)^{(1-y_i)}, \quad (8)$$

where N is the sample size and $S_i = S(\boldsymbol{\theta}, T_{\rm eff,i})$. The observation of whether an object is He-rich or H-rich is encapsulated with $y_i = 1$ for He-rich objects or $y_i = 0$ for H-rich objects. The optimization is made more straightforward by maximizing the natural logarithm of this quantity:

$$\log L(\boldsymbol{\theta}|T_{\rm eff}) = \sum_{i=1}^{N} \log(S_i) + \sum_{i=1}^{N} \log(1 - S_i). \quad (9)$$

Equivalently, one can minimize the negative log likelihood to find the best-fitting parameters. The optimization was performed using the Nelder–Mead algorithm built into the *minimize* function of SCIPY that uses a simplex to find the minimum gradient in the parameter space (Jones et al. 2001).

The best-fitting parameters for θ_0, θ_1, and θ_2 were 0.010 ± 0.007, -0.43 ± 0.20, and 2.57 ± 1.26, respectively. The logistic curve with these parameters is shown in Fig. 9 with the 1σ and 2σ confidence intervals shown in grey. The detections of He-rich or H-rich white dwarfs are shown in blue on the top and bottom axes, respectively. For comparison, we show again the values from the histogram bin method presented earlier (Fig. 8) in black circles. We remind the reader that the logistic curve is not a fit to the black points, but derived independently as discussed via the method of logistic regression. On the statistical significance of the increase of the He-fraction, an inspection of the best-fitting logistic function at 17 000 and 9 500 K finds that the increasing He-fraction across this temperature range can be considered a 5σ result.

Looking only at the histogram points, we find that for $20\,000 \geq T_{\rm eff}/[{\rm K}] \geq 14\,000$ the percentage of helium-dominated atmospheres lies between 10 and 20 per cent, with the general trend increasing by approximately 5 per cent towards the low-

temperature end of this interval, although we note that this is only a 1σ result, given the size of the error bars from Poisson errors. At lower effective temperatures, $13\,000 \geq T_{\rm eff}/[{\rm K}] \geq 10\,000$, we find a more significant increase, resulting in a final percentage of helium-dominated atmospheres of 35–40 per cent.

4.2 Mass distribution of thin hydrogen shells

The hypothesis being tested is whether the inverse proportionality between effective temperature and the relative number of helium-atmosphere white dwarfs is due to convective mixing or convective dilution.

Convective mixing, also referred to as dredge-up, is the process by which deeper material is dragged up by convective motions near the base of the (in this case hydrogen) convection zone. If the hydrogen convection zone is sufficiently close to the chemical boundary between the hydrogen and helium layers the material dragged up will be helium, and thus the two elements will mix.

Convective dilution describes the interaction of the top of the helium convection zone with a thin hydrogen shell located above. As the upper boundary of the convection zone reaches the hydrogen layer the hydrogen will be steadily incorporated into the helium convection zone.

Our first hypothesis is that the observed change in He-rich fraction is caused by convective mixing alone. As the helium envelope is typically orders of magnitude more massive (Iben & Renzini 1983; Romero et al. 2019), the prediction is that this runaway process quickly leaves a trace amount of hydrogen in a predominantly helium atmosphere (Rolland et al. 2018). Furthermore, convective motions in He-rich envelopes are many orders of magnitude faster (Fontaine & van Horn 1976) than any microscopic diffusion process that could separate helium and hydrogen (Koester 2009); hence, we assume this transition to be permanent. In this picture, we predict that the objects that change to appear helium dominated are white dwarfs with a total mass of hydrogen equal to the size of the convectively mixed region (i.e. convection zone size for chemical mixing) for a DA white dwarf at that temperature. Across the temperature range, this allows us to predict the total hydrogen mass for a percentage of the total white dwarf population within 133 pc. For DA stars that do not mix, we can only estimate the minimum mass of hydrogen.

To parametrize the convectively mixed region as a function of effective temperature, we turn to previous results from 3D radiation-hydrodynamic simulations (Cunningham et al. 2019). Fig. 10 shows the predicted mass of hydrogen being mixed convectively. Results from 3D numerical simulations for white dwarfs in the temperature range of $11\,400 \leq T_{\rm eff}/[{\rm K}] \leq 18\,000$ are shown in solid blue, where the multidimensional treatment allows for the inclusion of convective overshoot without employing free-parameters. Mixing-length theory mixed masses taken from Koester (2009), with updated tables, are shown in dotted red. Cunningham et al. (2019) found that the mixed mass can be increased by 2.5 dex when convective overshoot is accounted for in these hydrogen atmosphere white dwarfs.

We show our derived total mass of hydrogen for white dwarfs within 133 pc in Fig. 11 as a percentage of the total sample. Similarly to Fig. 10, results are given for the convectively mixed mass with (blue) and without (red, dotted) the inclusion of convective overshoot. To derive the histogram values, we sampled the parameter space of the function given in equation (6) using normally distributed parameters with means and standard deviations equal to the best-fitting parameters and their associated errors,

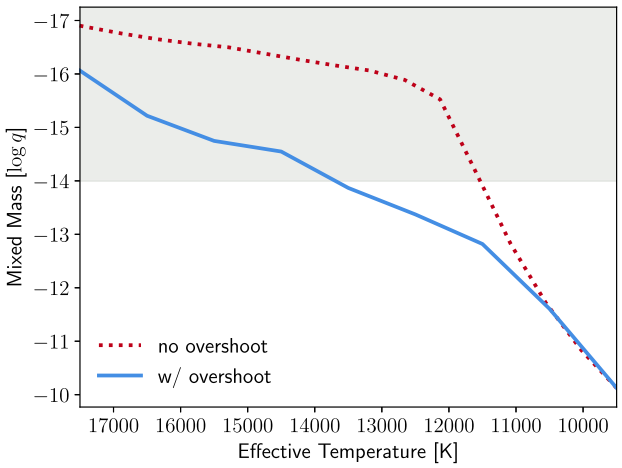

Figure 10 Temperature dependence of the fractional mass ($q = M_{\rm H}/M_{\rm WD}$) of the convectively mixed region in a DA white dwarf. Results are shown for mixed masses derived from 3D simulations (Cunningham et al. 2019, blue solid) and 1D MLT (ML2/$\alpha = 0.8$) with the convection zone defined by the Schwarschild criterion (Koester 2009, red dotted). In this work, we assume that when convective mixing occurs with the underlying helium layer, the mixed mass of hydrogen is equal to the total hydrogen mass in the star. The region in grey corresponds to hydrogen shell masses, where convective dilution is expected to proceed (Genest-Beaulieu & Bergeron 2019b).

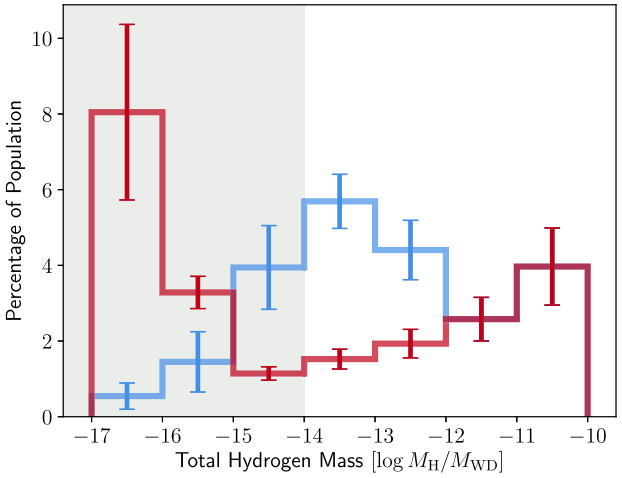

Figure 11 Percentage of white dwarfs with a given total hydrogen mass inferred from the percentage change of He-dominated white dwarfs (see Fig. 9). Results are shown for the two mixed mass prescriptions described in Fig. 10 with 3D and 1D results in blue and red, respectively. The sum is less than 100 per cent because we do not include white dwarfs with lower or upper limits on the total hydrogen masses (see Section 5). The region in grey corresponds to hydrogen shell masses that are *forbidden* for DA white dwarfs in our studied $T_{\rm eff}$ range according to convective dilution studies (Genest-Beaulieu & Bergeron 2019b). Under that scenario, these objects would evolve as He-rich white dwarfs and show no spectral change in our studied $T_{\rm eff}$ range.

respectively. The histogram values presented are the mean of the 10 000 histograms calculated and the error is the standard deviation around that mean.

We find that including the larger mixed masses borne from the convective overshoot results increases the inferred total mass of hydrogen for $\approx$ 15 per cent of the population by 2 dex. An increase in mixed mass due to convective overshoot is expected for

$T_{\rm eff} < 11\,400$ K but is currently not accessible directly from 3D numerical simulations. As such no difference is accounted for in the current model for total hydrogen masses above $M_{\rm H}/M_{\rm WD} \approx 10^{-12}$ because of the convergence of 3D and 1D results at lower temperatures (see Fig. 10).

The second hypothesis includes the possibility of convective dilution occurring. We use results from Genest-Beaulieu & Bergeron (2019b) that predict that convective dilution will occur in white dwarfs with a thin hydrogen shell of mass of $\log M_{\rm H}/M_{\rm WD} < -14.0$ when they cool to $T_{\rm eff} \approx 25\,000$ K. The inference is that these thinnest hydrogen shells are unlikely to exist by the time the white dwarf reaches $T_{\rm eff} < 20\,000$ K. More massive hydrogen layers are predicted to suppress convection in the underlying helium layer, preventing convective dilution, and allowing the hydrogen and helium shells to remain stratified down to lower effective temperatures or until convective mixing happens. In this scenario, convective mixing can therefore only occur in white dwarfs with total hydrogen masses $\log M_{\rm H}/M_{\rm WD} > -14$. Fig. 10 shows the region where convective dilution would have already happened in grey. In other words, convective mixing is only permitted for white dwarfs with $T_{\rm eff} < 13\,750$ K in the 3D picture or $T_{\rm eff} < 11\,500$ K in the 1D picture.

In Fig. 9, the temperature dependence of the helium-rich percentage appears to follow a steeper gradient for $T_{\rm eff} \lessapprox 14\,000$ K, whilst a zero gradient could be used to fit the behaviour of the percentage for $T_{\rm eff} > 14\,000$ K. This interpretation supports the hypothesis that convective dilution has already occurred in objects with $\log M_{\rm H}/M_{\rm WD} < -14.0$ by $T_{\rm eff} = 20\,000$ K and the next available mechanism for spectral evolution is the onset of convective mixing at $T_{\rm eff} \approx 14\,000$ K.

Fig. 11 also includes the region of stratified hydrogen masses *forbidden* by convective dilution in grey. It shows that, in this scenario, approximately half of the thin hydrogen shell masses predicted using 1D models of convection would be ruled out as non-physical at the $T_{\rm eff}$ values of interest. So too would a quarter of the inferred hydrogen shell masses in the 3D picture. The fewer non-physical predictions of the latter model suggests the 3D overshoot picture provides a more robust description of convection in these objects. Furthermore, for the 3D results we find that the two bins associated with the smallest total hydrogen mass are consistent with zero within 2σ. This provides evidence that the 3D overshoot model is in better agreement with the convective dilution model than a simple 1D treatment of convection alone. We note that the predictions of the convective dilution scenario are borne from a 1D mixing length treatment of convection. However, it was previously inferred that once the top of the helium layer becomes convectively unstable, a mechanism, that we suggest here is likely to be 3D convective overshoot, is able to dilute the top hydrogen layer into the helium convection zone (Rolland et al. 2018). As such 3D effects are already accounted implicitly in this scenario, although hydrodynamical simulations may give a more detailed picture of the onset of convective dilution, which is outside the scope of this work.

We will now go on to discuss the implications of these results for the evolution of white dwarfs and time-dependent accretion.

5 DISCUSSION

We have presented a statistical analysis of a sample of 1781 white dwarfs to extract the most accurate characterization of the fraction of He-rich white dwarfs as a function of temperature or cooling age. There is a highly statistically significant trend that the fraction of objects to have He-dominated atmospheres increases with cooling age. We find that this fraction increases from 10–20 per cent to 35–40 per cent between 20 000 and 9000 K, corresponding to cooling ages ranging from 60 to 800 Myr. The implementation of a rigorous optimization method allowed to constrain this increase continuously across the temperature range. When combined with our convective mixing model, this provided a mass distribution of thin hydrogen shells (total hydrogen mass in the star) as a percentage of the total white dwarf population. We now consider some of the implications of these results outside of the white dwarf sample directly considered in this paper.

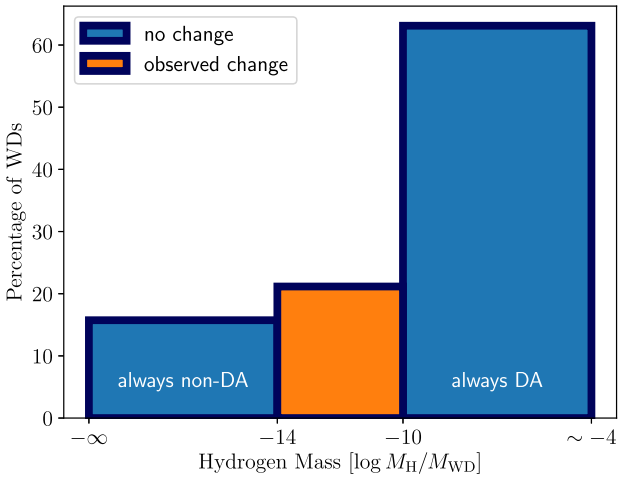

Figure 12 Percentage of white dwarfs with a given total hydrogen mass. The percentage observed to undergo a spectral change from DA to non-DA within the range of $20\,000 \geq T_{\rm eff}/[{\rm K}] \geq 9000$ are shown in orange. Those for which no change was observed within that range are shown in blue. Spectral evolution may be possible for temperatures outside of that range.

The He-rich fractions observed at 20 000 and 9000 K, respectively, allow for a mass distribution to be inferred across the full range of physically reasonable hydrogen shell masses. Fig. 12 shows this distribution for three bins. The central bin in orange comprises all objects observed to change from H- to He-rich in this study, where we use 3D convection for the hydrogen mass determination. The blue bins comprise all objects inferred to remain unchanged across the temperature range considered. We find that 61 per cent of white dwarfs must have a total hydrogen mass greater than $\log M_{\rm H}/M_{\rm WD} = -10$, and canonically it is considered that white dwarfs must have no more than $\log M_{\rm H}/M_{\rm WD} \approx -4$ (Romero et al. 2019).

At the other extreme of masses, we find that ~15 per cent of white dwarfs must have a total hydrogen mass less than $\log M_{\rm H}/M_{\rm WD} = -14$. We note that this mass is dictated by the mass limit found in the convective dilution studies of Rolland et al. (2018) and Genest-Beaulieu & Bergeron (2019b). These objects may have been DA stars at temperatures higher than 20 000 K. Our study cannot derive the total number of white dwarfs that spend their full evolution as He-rich atmospheres. For this result, spectral evolution must be studied directly at hotter and cooler temperatures.

5.1 Connecting with previous studies

The temperature range considered throughout this study was defined by the region where the Balmer lines have the greatest prominence. For cooler temperatures, this technique does not satisfactorily distinguish between H-rich and He-rich atmosphere white dwarfs. There have been recent efforts to quantify the ratio of DA to non-DA white dwarfs for cooler temperatures (Blouin et al. 2019).

Table 1. Fraction of helium-rich atmosphere white dwarfs ($N_{\text{He-atm}}/N_{\text{tot}}$) in the temperature range of 8000–7000 K presented in previous studies, collated by Blouin et al. (2019).

Study	$N_{\text{He-atm}}/N_{\text{tot}}$
Bergeron et al. (1997)	0.33 ± 0.12
Leggett et al. (1998)	0.45 ± 0.23
Bergeron et al. (2001)	0.37 ± 0.09
Tremblay & Bergeron (2008)	0.31 ± 0.06
Limoges et al. (2015)	0.23 ± 0.05
Blouin et al. (2019)	0.14 ± 0.03

We expect the contribution of convective mixing to the spectral evolution of white dwarfs to be less significant below 9000 K, as the size of the convection zone becomes less sensitive to effective temperature. This was evidenced in Blouin et al. (2019) where they observed a small change in He-rich fraction for white dwarfs with effective temperatures 8000–4000 K. Therefore, we would expect the He-rich fraction at the cooler end of our study to be somewhat comparable to the warmer end of the sample in their study. In Table 1, we show the fraction of He-rich white dwarfs between 8000 and 7000 K from literature values derived via various methods. To draw a comparison, we consider the results obtained for the objects with effective temperature in the range of 10 000–9000 K. The histogram method returned a He-rich fraction of 0.34 ± 0.03, whilst the logistic regression method found a He-rich fraction of 0.36 ± 0.02 at 9500 K, i.e. in the centre of that temperature bin. We find our results to be in agreement within 1σ with four earlier studies (Bergeron et al. 1997; Leggett et al. 1998; Bergeron et al. 2001; Tremblay & Bergeron 2008). In contrast, Limoges et al. (2015) and Blouin et al. (2019) find lower He-fractions. These differences could be investigated in the future with volume-complete spectroscopic follow-ups of local *Gaia* white dwarfs.

5.2 Hydrogen abundance in DBA white dwarfs

The origin of hydrogen in DB(A) white dwarfs above 9000 K (Rolland et al. 2018) can be reviewed in light of our improved description of the scenario of convective mixing. In Fig. 13, we plot in black circles the observed surface hydrogen abundance in a sample of 79 He-rich white dwarfs from Rolland et al. (2018). Open circles correspond to upper limits inferred from a non-detection of hydrogen.

For each effective temperature, the convective mixing scenario predicts a mass of hydrogen that gets mixed with the underlying helium layer. Since this mass increases with decreasing T_{eff}, at any given temperature, the maximum amount of hydrogen possible in a DB(A) white dwarf is for an object that has just experienced mixing. Lower hydrogen abundances are possible for DB(A) stars that have mixed at higher temperatures. We restrict our discussion to this upper limit of hydrogen in DB(A) stars.

For the mass of the helium convection zone, we use the results of a grid of 3D simulations of DBA white dwarfs (Cukanovaite et al. 2019). These simulations do not include a parametrization for (helium) convective overshoot, since DB(A) stars in that temperature range have deep convection zones for which a direct simulation is not yet possible. Including overshoot would result in larger helium convection zones, and therefore smaller upper limits on the surface abundance of hydrogen. This grid is interpolated iteratively so that the final surface hydrogen abundance is taken into account for the size of the convection zone.

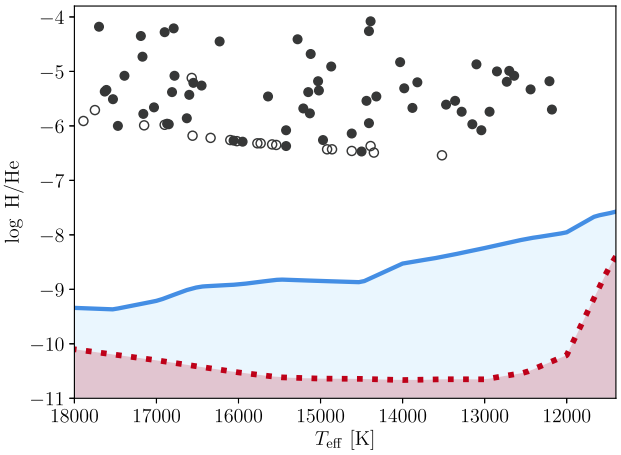

Figure 13 Observed hydrogen abundances in DB(A) white dwarfs drawn from the spectroscopic observations of Rolland et al. (2018). Filled circles show detections, whilst open circles designate upper limits based on a non-detection of hydrogen lines. Theoretical upper limits calculated using the overshoot model of Cunningham et al. (2019) shown in blue, and limits using 1D convection (Koester 2009) are shown in red dashed. Shaded regions correspond to H abundances that could be explained by convective mixing in either the 3D overshoot (blue) or no overshoot (red) models. All observed H-abundances are well outside the range predicted by these models.

The red, dashed line in Fig. 13 shows the predicted abundance of hydrogen in a He-rich white dwarf after convective mixing has occurred assuming a 1D mixed mass. The blue line shows the same quantity with the inclusion of the larger mixed mass from convective overshoot (Cunningham et al. 2019). In both cases, the calculation assumes that the hydrogen is homogeneously mixed into a larger He-rich convection zone.

The shaded regions beneath these upper limits can be considered the region in which all observations should lie if explained only by convective mixing. We note that the scenario of convective dilution predicts even smaller hydrogen abundances (Genest-Beaulieu & Bergeron 2019b). The entire observed sample of Rolland et al. (2018) lies well outside of these regions, with hydrogen abundances being ≈3–5 dex higher than the upper limit derived from 3D overshoot results. It seems clear that another mechanism must be invoked to explain these hydrogen abundances. 3D effects are clearly not able to provide a better fit to the observed hydrogen abundances. We favour the accretion of planetesimals as the most likely source of the observed hydrogen.

In principle, hydrogen accretion could cause a reverse change from He- to H-dominated atmospheres. However, recent studies on the spectral evolution of helium atmosphere white dwarfs and their accretion of hydrogen have suggested that this is an extremely rare scenario (Gentile Fusillo et al. 2017; Rolland et al. 2018). As such our assumption that the relative number of helium-atmosphere white dwarfs should increase monotonically with cooling age is likely a robust one.

6 CONCLUSIONS

We have presented a statistically significant ($>5\sigma$) detection of white dwarfs undergoing a transition from hydrogen-dominated to helium-dominated atmospheres, as they cool across the effective temperature range 20 000–9000 K. This was done using the largest volume-limited sample (133 pc) of white dwarfs for any previous study of this kind, with the precise determinations of effective

temperature utilizing *Gaia* photometry. We have characterized the temperature dependence of the rate of spectral evolution and used the most current grid of convection zone sizes for DA white dwarfs to determine the distribution of total hydrogen masses in white dwarfs. We find that the observed distribution of hydrogen shells in the white dwarf population peaks in the range of $\log M_{\rm H}/M_{\rm WD}$ from -10 to -4, with 60 per cent of all objects found within that range. Another 25 per cent of white dwarfs have thin hydrogen masses in the range $-14 < \log M_{\rm H}/M_{\rm WD} < -10$, and finally, 15 per cent have even thinner hydrogen masses ($\log M_{\rm H}/M_{\rm WD} < -14$).

These results have implications for models of pulsations in white dwarfs, stellar evolution – in particular during the AGB – and the accretion of material after the formation of white dwarfs. In the future, volume-complete spectroscopic samples will be able to increase the range in mass for which we can constrain the total amount of hydrogen in a white dwarf.

ACKNOWLEDGEMENTS

This work has made use of data from the European Space Agency (ESA) mission *Gaia* (https://www.cosmos.esa.int/gaia), processed by the *Gaia* Data Processing and Analysis Consortium (DPAC; https://www.cosmos.esa.int/web/gaia/dpac/consortium). Funding for the DPAC has been provided by national institutions, in particular the institutions participating in the *Gaia* Multilateral Agreement.

Funding for SDSS-III has been provided by the Alfred P. Sloan Foundation, the Participating Institutions, the National Science Foundation, and the U.S. Department of Energy Office of Science. The SDSS-III web site is http://www.sdss3.org/.

SDSS-III is managed by the Astrophysical Research Consortium for the Participating Institutions of the SDSS-III Collaboration including the University of Arizona, the Brazilian Participation Group, Brookhaven National Laboratory, Carnegie Mellon University, University of Florida, the French Participation Group, the German Participation Group, Harvard University, the Instituto de Astrofisica de Canarias, the Michigan State/Notre Dame/JINA Participation Group, Johns Hopkins University, Lawrence Berkeley National Laboratory, Max Planck Institute for Astrophysics, Max Planck Institute for Extraterrestrial Physics, New Mexico State University, New York University, Ohio State University, Pennsylvania State University, University of Portsmouth, Princeton University, the Spanish Participation Group, University of Tokyo, University of Utah, Vanderbilt University, University of Virginia, University of Washington, and Yale University.

The research leading to these results has received funding from the European Research Council under the European Union's Horizon 2020 research and innovation programme no. 677706 (WD3D).

REFERENCES

Althaus L. G., Córsico A. H., Bischoff-Kim A., Romero A. D., Renedo I., García-Berro E., Miller Bertolami M. M., 2010, ApJ, 717, 897
Althaus L. G., Camisassa M. E., Miller Bertolami M. M., Córsico A. H., García-Berro E., 2015, A&A, 576, A9
Baglin A., Vauclair G., 1973, A&A, 27, 307
Bergeron P., Ruiz M. T., Leggett S. K., 1997, ApJS, 108, 339
Bergeron P., Leggett S. K., Ruiz M. T., 2001, ApJS, 133, 413
Bergeron P., Dufour P., Fontaine G., Coutu S., Blouin S., Genest-Beaulieu C., Bédard A., Rolland B., 2019, ApJ, 876, 67
Blanton M. R. et al., 2017, AJ, 154, 28
Blouin S., Dufour P., Thibeault C., Allard N. F., 2019, ApJ, 878, 63
Bradley P. A., 1996, ApJ, 468, 350
Brickhill A. J., 1983, MNRAS, 204, 537
Brickhill A. J., 1991, MNRAS, 251, 673
Camarota L., Holberg J. B., 2014, MNRAS, 438, 3111
Chayer P., 2014, MNRAS, 437, L95
Chen E. Y., Hansen B. M. S., 2012, ApJ, 753, L16
Chromey A., 2019, 36th Int. Cosmic Ray Conf. (ICRC2019), Madison, WI
Coutu S., Dufour P., Bergeron P., Blouin S., Loranger E., Allard N. F., Dunlap B. H., 2019, ApJ, 885, 74
Cukanovaite E., Tremblay P. E., Freytag B., Ludwig H. G., Bergeron P., 2018, MNRAS, 481, 1522
Cukanovaite E., Tremblay P. E., Freytag B., Ludwig H. G., Fontaine G., Brassard P., Toloza O., Koester D., 2019, MNRAS, 490, 1010
Cummings J. D., Kalirai J. S., Tremblay P.-E., Ramirez-Ruiz E., Bergeron P., 2016, ApJ, 820, L18
Cunningham T., Tremblay P.-E., Freytag B., Ludwig H.-G., Koester D., 2019, MNRAS, 488, 2503
D'Antona F., Mazzitelli I., 1990, ARA&A, 28, 139
De Gerónimo F. C., Althaus L. G., Córsico A. H., Romero A. D., Kepler S. O., 2018, A&A, 613, A46
Eisenstein D. J. et al., 2006, ApJS, 167, 40
Farihi J., Brinkworth C. S., Gänsicke B. T., Marsh T. R., Girven J., Hoard D. W., Klein B., Koester D., 2011, ApJ, 728, L8
Fontaine G., Brassard P., 2008, PASP, 120, 1043
Fontaine G., van Horn H. M., 1976, ApJS, 31, 467
Fontaine G., Wesemael F., 1987, in Philip A. G. D., Hayes D. S., Liebert J. W., eds, IAU Colloq. 95: Second Conference on Faint Blue Stars, L. Davis Press, Schenectady, NY. p. 319
Fontaine G., Brassard P., Bergeron P., 2001, PASP, 113, 409
Gaia Collaboration et al., 2016, A&A, 595, A1
Gaia Collaboration et al., 2018, A&A, 616, A1
Genest-Beaulieu C., Bergeron P., 2019a, ApJ, 871, 169
Genest-Beaulieu C., Bergeron P., 2019b, ApJ, 882, 106
Gentile Fusillo N. P. et al., 2019, MNRAS, 482, 4570
Gentile Fusillo N. P., Gänsicke B. T., Greiss S., 2015, MNRAS, 448, 2260
Gentile Fusillo N. P., Gänsicke B. T., Farihi J., Koester D., Schreiber M. R., Pala A. F., 2017, MNRAS, 468, 971
Giammichele N., Fontaine G., Brassard P., Charpinet S., 2016, ApJS, 223, 10
Herwig F., Blöcker T., Langer N., Driebe T., 1999, A&A, 349, L5
Hollands M. A., Koester D., Alekseev V., Herbert E. L., Gänsicke B. T., 2017, MNRAS, 467, 4970
Hollands M. A., Tremblay P. E., Gänsicke B. T., Gentile-Fusillo N. P., Toonen S., 2018, MNRAS, 480, 3942
Hummer D. G., Mihalas D., 1988, ApJ, 331, 794
Iben I. J., Renzini A., 1983, ARA&A, 21, 271
Jones E. et al., 2001, SciPy: Open Source Scientific Tools for Python. Available at: http://www.scipy.org/
Kalirai J. S., 2012, Nature, 486, 90
Kepler S. O. et al., 2019, MNRAS, 486, 2169
Kilic M., Bergeron P., Dame K., Hambly N. C., Rowell N., Crawford C. L., 2019, MNRAS, 482, 965
Koester D., 1976, A&A, 52, 415
Koester D., 2009, A&A, 498, 517
Koester D., Kepler S. O., 2019, A&A, 628, A102
Koester D., Gänsicke B. T., Farihi J., 2014, A&A, 566, A34
Leggett S. K., Ruiz M. T., Bergeron P., 1998, ApJ, 497, 294
Limoges M. M., Bergeron P., Lépine S., 2015, ApJS, 219, 19
MacDonald J., Vennes S., 1991, ApJ, 371, 719
Miller Bertolami M. M., 2016, A&A, 588, A25
Morrissey P. et al., 2007, ApJS, 173, 682
Ourique G., Romero A. D., Kepler S. O., Koester D., Amaral L. A., 2019, MNRAS, 482, 649
Pelletier C., Fontaine G., Wesemael F., Michaud G., Wegner G., 1986, ApJ, 307, 242
Raddi R., Gänsicke B. T., Koester D., Farihi J., Hermes J. J., Scaringi S., Breedt E., Girven J., 2015, MNRAS, 450, 2083
Rolland B., Bergeron P., Fontaine G., 2018, ApJ, 857, 56
Romero A. D. et al., 2017, ApJ, 851, 60

Romero A. D., Kepler S. O., Joyce S. R. G., Lauffer G. R., Córsico A. H., 2019, MNRAS, 484, 2711
Schatzman E., 1945, Ann. d'Astrophys., 8, 143
Schoenberner D., Weidemann V., 1983, in Aller L. H., ed., Proc. IAU Symp. Vol. 103, Planetary Nebulae, Dordrecht: Reidel. p. 359
Shipman H. L., 1972, ApJ, 177, 723
Sion E. M., 1984, ApJ, 282, 612
Straniero O., Domínguez I., Imbriani G., Piersanti L., 2003, ApJ, 583, 878
Strittmatter P. A., Wickramasinghe D. T., 1971, MNRAS, 152, 47
Tremblay P. E. et al., 2017, MNRAS, 465, 2849
Tremblay P. E., Bergeron P., Gianninas A., 2011, ApJ, 730, 128
Tremblay P. E., Gianninas A., Kilic M., Ludwig H. G., Steffen M., Freytag B., Hermes J. J., 2015, ApJ, 809, 148
Tremblay P.-E., Bergeron P., 2008, ApJ, 672, 1144
Tremblay P.-E., Ludwig H.-G., Steffen M., Freytag B., 2013, A&A, 559, A104
Tremblay P.-E., Kalirai J. S., Soderblom D. R., Cignoni M., Cummings J., 2014, ApJ, 791, 92
Tremblay P.-E., Cummings J., Kalirai J. S., Gänsicke B. T., Gentile-Fusillo N., Raddi R., 2016, MNRAS, 461, 2100
Tremblay P.-E., Cukanovaite E., Gentile Fusillo N. P., Cunningham T., Hollands M. A., 2019, MNRAS, 482, 5222
Wall R. E., Kilic M., Bergeron P., Rolland B., Genest-Beaulieu C., Gianninas A., 2019, MNRAS, 489, 5046
Werner K., Herwig F., 2006, PASP, 118, 183
Werner K., Rauch T., Kruk J. W., 2018, A&A, 609, A107
Winget D. E., Hansen C. J., Liebert J., van Horn H. M., Fontaine G., Nather R. E., Kepler S. O., Lamb D. Q., 1987, ApJ, 315, L77
Wood M. A., 1990, JRASC, 84, 150
Zuckerman B., Koester D., Melis C., Hansen B. M., Jura M., 2007, ApJ, 671, 872